CHINA COMMUNICATIONS

The Resource Allocation for Secure SWIPT Network Aided by Reconfigurable Intelligent Surface Relying on S-parameter Communication Model

Ruoyan Ma[1], Jie Tang[1,*], Xiu Yin Zhang[1], Kai-Kit Wong[2], Jonathon A. Chambers[3]

[1] School of Electronic and Information Engineering, South China University of Technology, Guangzhou 510641, China
[2] Department of Electronic and Electrical Engineering, University College London, WClE 6BT London, U.K
[3] University of Leicester, Leicester LE1 7RH, U.K
[*] The corresponding author, email: eejtang@scut.edu.cn

Abstract: In future Internet of Things (IoT) based scenarios, the network may encounter significant issues related to energy and communication as a result of progressively growing terminals. We introduce simultaneous wireless power transfer (SWIPT) technology assisted by the reconfigurable intelligent surface (RIS) to counteract this challenge. Consequently, the network's flexibility and reliability will be further enhanced. According to this system architecture, the scattering-parameter-based communication model is introduced to disclose hardware features for an energy efficiency (EE) maximization problem. Specifically, the potential unauthorized demodulation is also considered in the problem formulation. To resolve the issue, an alternative strategy is utilized to optimize the coupled variables iteratively. Especially, the BCD approach based on the Sherman-Morrison formula is proposed to solve the subproblem for RIS. The numerical results demonstrate the physical characteristics of the hardware cannot be dismissed lightly. Besides, the configuration of the RIS may impact the network performance directly.

Keywords: S-parameter; electromagnetic system model;simultaneous wireless information and power transfer; reconfigurable intelligent surface; energy efficiency.

Received: XXX
Revised: XXX
Editor: XXX

I. INTRODUCTION

The Internet of Things (IoT) is the backbone technology for conducting the digital revolution. With the support of it, a denser interconnection has been built between people and things. Particularly, seamlessly connected networks enable further upgrading of production automation [1]. Moreover, blueprints for human-centered smart cities will become more feasible. As a result, the high efficiency of production and the convenience of life make it possible for the economy and society to leap forward [2]. Nevertheless, the increasing number of terminal accesses causes difficulty in maintaining the reliability of communication. Especially, there is a high probability of communication outage at the terminals due to their limited power supply. Thus, the introduction of a technology that guarantees reliable information transfer while offering a flexible energy supply is essential [3].

Fortunately, the simultaneous wireless information and power transfer (SWIPT) system can satisfy the requirements of communication and power supply at the same time. Particularly, terminal devices may continually harvest energy for their own consumption as long as there are enough electromagnetic waves available. Indeed, this condition can be realized easily in IoT scenarios owing to the constantly generated wireless signals [4]. From the perspective of system architecture, the receiving subsystem of SWIPT can be categorized into dual-demand and single-demand types [3]. The

dual-demand one refers to that the information demodulation (ID) and energy harvesting (EH) should be met simultaneously. Single-demand form implies that only one of their requirements needs to be satisfied. Indeed, these two structures have distinct application scenarios. However, there still remains an issue of supporting reliable services, since these structures are both sensitive to the blocks of transmission.

To properly address this issue, the reconfigurable intelligent surface (RIS) can be introduced. With this technology, the stability of SWIPT transmission will be enhanced [5]. In particular, the RIS is able to reconstruct the obstructed channels with its controllability. During the operation, the RIS can configure its controller to adjust the status of the elements in the array [1]. Consequently, the incident waves can be reflected in the desired direction. The regulation level of the reflected wave is discrete or continuous depending on whether the circuit uses a positive-intrinsic-negative (PIN) diode or varactor [6]. In addition, the whole process requires very low energy consumption, which means RIS can be seen as an energy-efficient technology [1]. Indeed, this is the main reason why RIS is considered as a key enabling technology for sixth-generation (6G) wireless communication technology.

Recently, a series of studies about the RIS-assisted SWIPT network have been conducted. In particular, these studies have different focal points in terms of the scenario configuration, architecture design, and problem formulation. As for the architecture of SWIPT, the dual-demand receiver (DDR) [3, 7–10] and single-demand receiver (Rx) [4, 5, 11–14] were adopted to serve the various needs of terminals. Specifically, the time-switching (TS) [7] and power-splitting (PS) [3, 8–10] strategies were introduced to separate the ID and EH streams for dual-demand terminals. Regarding the scenario configurations, the multiple-input multiple-output (MIMO) [4] and multiple-input multiple-output (MISO) [3, 5, 11–14] systems were analyzed. Relying on these basic settings, the unmanned aerial vehicle (UAV) [8], the rate-splitting multiple access (RSMA) [9], and the orbital angular momentum (OAM) [10] were introduced to consist of more complete application scenarios. Although the main quality of service (QoS) constraints are similar, the objectives were set differently for distinct performance priorities in problem formulations. Particularly, the sum-rate maximization [4], the harvested energy maximization[11], and the transmitting power minimization [5] were configured as objectives, respectively. Compared to the single objective, the study related to the multi-objective problem has also been researched. In addition, several novel RIS configurations such as active RIS [13] and simultaneously transmitting and reflecting RIS (STAR-RIS) [14] were also introduced into the SWIPT system.

Although there are numerous pieces of research about the RIS-aided SWIPT system, few of them take the physical features into account. Indeed, as an electromagnetic (EM) device, analyzing EM characteristics of RIS will make the related research closer to the actual situation [15]. From this point, several studies already have been tried to construct the practical RIS model. The circuit-based analysis was utilized to describe the physical features of RIS [16]. In detail, the inductance, capacitance, and resistance of RIS components were revealed apparently. Based on this, the actual expressions for the amplitude and phase shift were also presented. With the introduction of radar theory, the RIS can be seen as an anomalous reflection device and the phase shift was connected to the calculation of EM fields [17]. As a consequence, the EM information of the incident and reflection waves were shown in the modeling. Besides, [18] studied the reflection coefficients of RIS from the EM view. It demonstrated that the amplitude and phase shift of the RIS units have a direct relationship. In contrast to the above ideas, some works were conducted to build the system-level model for the RIS-assisted network. In particular, the impedance-based end-to-end communication model was introduced to prove the importance of mutual-coupling (MC) effects [15]. The results demonstrated that the unawareness of the hardware impact caused the performance gap in the system. Furthermore, the S-parameter-based analysis was used to expose the crucial characteristics of the main devices in the system [19]. Specifically, the communication model was constructed on the concept of the N-port network.

Motivated by the above studies, we research a MISO-downlink RIS-assisted SWIPT system in this paper. Additionally, the potential threat of information leakage is also considered for communication security. Furthermore, the whole system is built on a practical communication model, which is proposed from the S-parameter analysis. The main contributions are pre-

sented as following points:

- The S-parameters, which may be more suitable for analyzing the scattering properties of RIS [19], are employed to build the communication model. Based on this, the physical information of all the ends (i.e., Tx, Rx, and RIS) is included naturally and the configurations are not limited. Indeed, as long as the actual S-parameters at each end are known, the mismatching effect and MC effect can be introduced into the model. This is the foundation for conducting the subsequent practicality-oriented system analysis.
- Relying on the proposed communication model, the research about RIS-aided SWIPT network is further carried out. Particularly, there are two types of Rxs, which refer to the DDR and single-demand EH Rx (EHR). For separating the EH and ID parts of DDRs, the PS approach is adopted. Besides, EHRs may potentially be an eavesdropper to achieve unauthorized information. Concerning the reliability of the network, artificial noise (AN) is included in the system optimization to disturb the ID of EHRs.
- The energy efficiency (EE) maximization problem related to the above setting is then introduced. Within it, the coupled variables can be solved through the strategy of alternative optimization (AO). However, tackling the subproblem of RIS is very intractable due to the proposed communication model. To simplify it, the Sherman-Morrison formula is utilized to deconstruct the subproblem into a more solvable form. In the specific tackling process, the semi-definite relaxation (SDR), successive convex approximation (SCA), and Dinkelbach's algorithm are applied.
- The research about the QoS requirements and hardware configuration of RIS is presented in the numerical simulation. To show how the proposed model connects the practical hardware to system optimization, we first design an RIS device through the EM software. Then its S-parameter is introduced into the network analysis. The according outcomes demonstrate significant hardware characteristics of RIS do affect system performance directly.

The organization of the paper is presented as follows. In detail, the introduced system model is presented in section II. Furthermore, section III includes the problem of the RIS-assisted SWIPT secure network. To effectively resolve the proposed issue, the optimization strategy is provided in section IV. Then section V presents hardware-related numerical results. Finally, the conclusion is summarized in section VI.

The bold type of the lower-case $\mathbf{a}$ and upper-case $\mathbf{A}$ represents the vector and matrix. Further, the notations $\mathbf{I}$ and $\mathbf{0}$ denote the identity matrix and the zero matrix. Moreover, $\mathbf{A}^H$, $\|\mathbf{A}\|$, $\mathrm{Tr}(\mathbf{A})$, and $\mathrm{Rank}(\mathbf{A})$ are the Hermitian conjugate transpose, spectral norm, trace, and rank of the matrix $\mathbf{A}$. $\mathbf{A}_{[x,y]}$ represents the element in the x_{th} row and the y_{th} column. Besides, the semidefinite matrix is written as $\mathbf{A} \succeq 0$. $\mathrm{diag}(\mathbf{a})$ is presented for the diagonal matrix with the elements in $\mathbf{a}$. In addition, the $\mathbb{R}^{n\times m}$ and $\mathbb{C}^{n\times m}$ are utilized to denote the real matrix and the complex matrix.

II. THE PRACTICAL END-TO-END COMMUNICATION MODEL

We introduce the S-parameter theory to construct the end-to-end communication model as in [19]. Particularly, the S-parameter is a kind of scattering indicator, which is utilized to describe the relationship between the incident wave and the reflection wave in the radio frequency (RF) system [20]. Its general form can be written as

$$\mathbf{b} = \mathbf{S}\mathbf{a}, \tag{1}$$

where $\mathbf{S}$ represents the S-parameter of the RF system. Moreover, $\mathbf{b}$ and $\mathbf{a}$ are the reflection wave and incident wave attached to the system. With the idea of the S-parameter, the transmission features among all ends can be presented. In the specific analysis process, we first study the end-level model and then connect them together to build the system-level RIS-assisted communication model. At each end, the model construction relies on the circuit characteristics. As for the RIS and Rx, the circuits are simplified as load-based forms [19]. It means that there is only a load connected to the RIS element and Rx antenna. Therefore, the relationships between incident waves and reflection waves are just related to the reflection coefficients of the loads. Their expressions can be shown as follows.

$$\mathbf{b}_I = \mathbf{\Theta}\mathbf{a}_I, \tag{2}$$

$$\begin{aligned}\mathbf{H}_{E2E}(\boldsymbol{\Theta}) =&(\boldsymbol{\Gamma}_R+\mathbf{I})(\mathbf{I}-\mathbf{S}_{RR}\boldsymbol{\Gamma}_R)^{-1}\mathbf{S}_{RT}(\mathbf{I}+\mathbf{S}_{TT})^{-1}\\ &+(\boldsymbol{\Gamma}_R+\mathbf{I})(\mathbf{I}-\mathbf{S}_{RR}\boldsymbol{\Gamma}_R)^{-1}\mathbf{S}_{RI}(\boldsymbol{\Theta}^{-1}-\mathbf{S}_{II})^{-1}\mathbf{S}_{IT}(\mathbf{I}+\mathbf{S}_{TT})^{-1},\end{aligned} \tag{8}$$

$$\mathbf{b}_R = \boldsymbol{\Gamma}_R\mathbf{a}_R. \tag{3}$$

Among them, $\boldsymbol{\Theta}$ and $\boldsymbol{\Gamma}_R$ are the diagonal reflection-coefficient matrices of loads in the RIS and Rx. Moreover, the dimensions of these matrices are the element numbers of the according end. Being different from them, the Tx circuit has the resource instead of the load. Accordingly, its end-level model is presented as the following equation.

$$\mathbf{a}_T = \mathbf{b}_s + \boldsymbol{\Gamma}_{s,T}\mathbf{b}_T, \tag{4}$$

where $\mathbf{b}_s$ denote the source wave and $\boldsymbol{\Gamma}_{s,T}$ refer to the diagonal reflection-coefficient matrix of the source.

Based on the above end-level models, we next analyze their transmission relationships to construct the end-to-end model. For each end, the basic idea is finding the influences from other ends to its waves. With this idea, we can achieve the following set of formulas.

$$\mathbf{a}_T = \mathbf{S}_{TT}\mathbf{b}_T, \tag{5}$$
$$\mathbf{a}_I = \mathbf{S}_{IT}\mathbf{b}_T + \mathbf{S}_{II}\mathbf{b}_I, \tag{6}$$
$$\mathbf{a}_R = \mathbf{S}_{RT}\mathbf{b}_T + \mathbf{S}_{RI}\mathbf{b}_I + \mathbf{S}_{RR}\mathbf{b}_R, \tag{7}$$

where $\mathbf{S}_{TT}$, $\mathbf{S}_{II}$, and $\mathbf{S}_{RR}$ are the self S-parameter of the Tx, RIS, and Rx. It is worth mentioning that their diagonal elements are reflection coefficients of array units and the off-diagonal elements denote the mutual coupling (MC) values, which come from the coupling excitation between the elements. Besides, $\mathbf{S}_{AB}$, where $A, B \in \{T, I, R\}$, represents the transmission factors from the end B and to the end A. Moreover, we omit the back transmission factors $\mathbf{S}_{TR}$, $\mathbf{S}_{TI}$, and $\mathbf{S}_{IR}$ due to their negligible influence in the downlink far-field RIS-based network.

With the equations (2)-(7), we can further achieve the end-to-end transmission matrices $\mathbf{H}_{E2E}$ between the Tx voltages $\mathbf{v}_T$ and the Rx voltage $\mathbf{v}_R$ as in (8). Particularly, $\mathbf{v}_T = \mathbf{a}_T + \mathbf{b}_T$ and $\mathbf{v}_R = \mathbf{a}_R + \mathbf{b}_R$. Specifically, the proposed model $\mathbf{H}_{E2E}$ includes the crucial hardware features, such as mismatching impacts and MC effects, of all the ends. Besides, it is also convenient to insert more factors brought by the other RF devices (e.g., power amplifier, low-noise amplifier, and matching circuit). As a result, more physical properties can be incorporated into the analysis by building the problem formulation with $\mathbf{H}_{E2E}$.

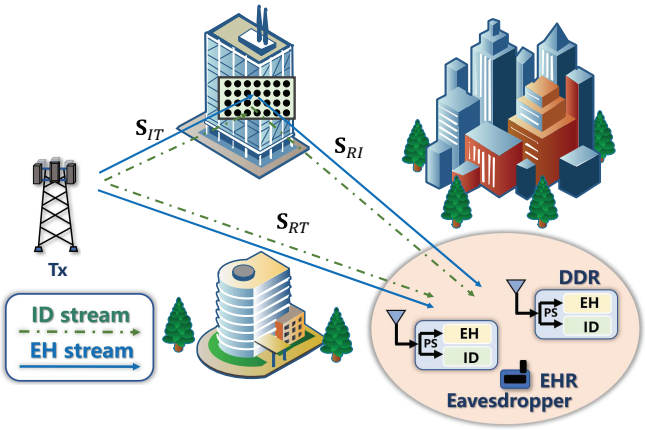

Figure 1. *The scenario of the downlink MISO RIS-assisted SWIPT system.*

III. THE PROBLEM FORMULATION

The scenario of the RIS-assisted SWIPT network is presented in Figure 1. In particular, the Tx is configured by an array with N_T antennas and all the Rxs are single-antenna systems. Moreover, there are two kinds of users (i.e., DDR and EHR). The DDR utilizes the PS strategy to split the ID and EH streams. As the Rxs are sensitive to the quality of the transmission, the RIS with N_I elements is introduced to improve their service stability. According to the above MISO setting, we then generate the communication model $\mathbf{h} \in \mathbb{C}^{1\times N_T}$, which is simplified from the (9), as following

$$\mathbf{h}(\boldsymbol{\Theta}) = \mathbf{s}_{RT} + \mathbf{s}_{RI}(\boldsymbol{\Theta}^{-1} - \mathbf{S}_{II})^{-1}\mathbf{S}_{IT}, \tag{9}$$

where the characteristics of other ends are not considered as important as the hardware features of RIS, which is our primary focus in this study. Therefore, the matching conditions of the Tx array, Rx antenna, and Rx load are set perfectly. Moreover, the MC effects of the Tx array can be ignored due to the sufficient

$$P_{\mathrm{EH},n}^{(\mathrm{DDR})}\left(\mathbf{w}_n,\rho_n,\mathbf{\Theta},\mathbf{z}\right)=\left(1-\rho_n\right)\left(\mathbf{h}_n(\mathbf{\Theta})\left(\sum_{n=1}^{N_D}\mathbf{w}_n{\mathbf{w}_n}^H+\mathbf{z}\mathbf{z}^H\right)\mathbf{h}_n(\mathbf{\Theta})^H\right), \tag{14}$$

$$P_{\mathrm{DC},n}^{(\mathrm{DDR})}\left(\mathbf{w}_n,\rho_n,\mathbf{\Theta},\mathbf{z}\right)=\frac{v_{B,n}(1+\chi_n)}{\chi_n\left(1+\exp\left(-\kappa_n\left(P_{\mathrm{EH},n}^{(\mathrm{DDR})}\left(\mathbf{w}_n,\rho_n,\mathbf{\Theta},\mathbf{z}\right)-\varpi_n\right)\right)\right)}-\frac{v_{B,n}}{\chi_n}, \tag{15}$$

deployment space for decreasing the MC effect. Consequently, $\mathbf{\Gamma}_R$, $\mathbf{S}_{RR}$, and $\mathbf{S}_{TT}$ in (8) turn to identity matrices, which brings (9). With (9), we can present the received signals of the n^{th} DDR as following

$$y_n^{(\mathrm{DDR})}=\mathbf{h}_n(\mathbf{\Theta})\mathbf{x}+n_{a,n}, \tag{10}$$

where n_a represents the additive white Gaussian noise (AWGN) at the Rx antenna of the DDR. In particular, it follows the distribution as $n_{a,n}\sim\mathcal{CN}(0,\sigma_n^2)$, where σ_n^2 denote the variance. Moreover, transmitting signal $\mathbf{x}\in\mathbb{C}^{N_T\times 1}$ is denoted as

$$\mathbf{x}=\sum_{n=1}^{N_\mathrm{D}}\mathbf{w}_n s_n+\mathbf{z}, \tag{11}$$

in which, $\mathbf{w}_n$ is the active beamforming vector and s_n is the signal, which is demanded by N_D DDRs, satisfies the distribution as $s_n\sim\mathcal{CN}(0,1)$. Furthermore, although the EHR in Figure 1 only has the requirement for power supply, it has the possibility to decode the information assigned to the DDR unauthorizedly. As a result, we introduce the artificial noise vector $\mathbf{z}$ to interrupt this potential eavesdropping.

Relying on the signal model in (10), the ID part through the PS scheme can be written as

$$y_{\mathrm{ID},n}^{(\mathrm{DDR})}=\sqrt{\rho_n}y_n+n_{p,n}, \tag{12}$$

where ρ_n is the PS ratio and n_p represents the signal-processing noise, which follows the distribution as $n_{p,n}\sim\mathcal{CN}(0,\delta_n^2)$. Then the signal-to-interference plus noise ratio (SINR) of the n^{th} DDR can be presented as the following expression.

$$\gamma_n^{(\mathrm{DDR})}\left(\mathbf{w}_n,\rho_n,\mathbf{\Theta},\mathbf{z}\right)=\frac{\left|\mathbf{h}_n(\mathbf{\Theta})\mathbf{w}_n\right|^2}{\left|\mathbf{h}_n(\mathbf{\Theta})\mathbf{z}\right|^2+\sum_{k\neq n}^{N_D}\left|\mathbf{h}_n(\mathbf{\Theta})\mathbf{w}_k\right|^2+\sigma_n^2+\frac{\delta_n^2}{\rho_n}}, \tag{13}$$

Accordingly, the EH power for the DDR with $(1-\rho_n)$ ratio is shown as in (14), where the noise power is ignored owing to its negligible value. Indeed, the equation (14) still represents the RF power, which needs to be rectified to the direct-current (DC) power. To achieve this goal, the rectifying circuit, which consists of the diode, should be adopted. During the rectifying, the input-to-output power relationship is nonlinear. Particularly, the output DC power can be given as in (15), where $v_{B,n}$ denotes the saturated power related to the diode. Moreover, $\chi_n=\exp(\kappa_n\varpi_n)$, where κ_n and ϖ_n are the circuit parameters of the n^{th} DDR.

Similar to the above formulas, the EH power of the l^{th} EHR is given as

$$P_{\mathrm{EH},l}^{(\mathrm{EHR})}\left(\mathbf{w}_n,\mathbf{\Theta},\mathbf{z}\right)=\left(\mathbf{h}_l(\mathbf{\Theta})\left(\sum_{n=1}^{N_D}\mathbf{w}_n{\mathbf{w}_n}^H+\mathbf{z}\mathbf{z}^H\right)\mathbf{h}_l(\mathbf{\Theta})^H\right). \tag{16}$$

The $P_{\mathrm{DC},l}^{(\mathrm{EHR})}\left(\mathbf{w}_n,\mathbf{\Theta},\mathbf{z}\right)$ follows the similar form as (15), thus we omit its specific expression. In addition, the EHR may attempt to demodulate the unauthorized information from the DDRs. The SINR of the l^{th} EHR for receiving the information of the n^{th} DDR is

$$\gamma_{l,n}^{(\mathrm{DDR})}\left(\mathbf{w}_n,\mathbf{\Theta},\mathbf{z}\right)=\frac{\left|\mathbf{h}_l(\mathbf{\Theta})\mathbf{w}_n\right|^2}{\left|\mathbf{h}_l(\mathbf{\Theta})\mathbf{z}\right|^2+\sum_{k\neq n}^{N_D}\left|\mathbf{h}_l(\mathbf{\Theta})\mathbf{w}_k\right|^2+\sigma_l^2+\delta_l^2}, \tag{17}$$

As for the dissipated power P_{total} of the whole system, its specific form is presented as

$$P_{\mathrm{total}}\left(\mathbf{w}_n,\rho_n,\mathbf{\Theta},\mathbf{z}\right)=P_T+P_B+\epsilon\left(\sum_{n=1}^{N_D}R_n^{(\mathrm{DDR})}\left(\mathbf{w}_n,\rho_n,\mathbf{\Theta},\mathbf{z}\right)\right), \tag{18}$$

where P_T denotes the transmitting power, it can be calculated as $P_T=\sum_{n=1}^{N_\mathrm{D}}\left\|\mathbf{w}_n\right\|_2^2+\left\|\mathbf{z}\right\|_2^2$. Moreover, the

power consumption of devices is written as $P_B = P_c + N_I P_I$, where P_c and P_I represent the static dissipation of the hardware component and element-operation consumption of the RIS, respectively. Specifically, we also consider the power usage of the signal Processing as $\epsilon\left(\sum_{n=1}^{N_D} R_n^{(\mathrm{DDR})}\left(\mathbf{w}_n, \rho_n, \mathbf{\Theta}, \mathbf{z}\right)\right)$, where ϵ is utilized to express the power input per unit rate and data rate is shown as $R_n^{(\mathrm{DDR})}\left(\mathbf{w}_n, \rho_n, \mathbf{\Theta}, \mathbf{z}\right) = \log_2\left(1+\gamma_n^{(\mathrm{DDR})}\left(\mathbf{w}_n, \rho_n, \mathbf{\Theta}, \mathbf{z}\right)\right)$.

In this paper, we focus on the EE performance of the network, which means that both the data rate and power dissipation should be balanced. Specifically, the expression of the EE can be shown as

$$\mathrm{EE}\left(\mathbf{w}_n, \rho_n, \mathbf{\Theta}, \mathbf{z}\right) = \frac{\sum_{n=1}^{N_D} R_n^{(\mathrm{DDR})}\left(\mathbf{w}_n, \rho_n, \mathbf{\Theta}, \mathbf{z}\right)}{P_{\text{total}}\left(\mathbf{w}_n, \rho_n, \mathbf{\Theta}, \mathbf{z}\right)}. \tag{19}$$

Based on the above equations, we then propose the EE maximization problem subject to the QoS requirements and physical restriction as follows

$$\mathbf{P}_0: \max_{\{\mathbf{w}_n, \rho_n, \mathbf{\Theta}, \mathbf{z}\}} \mathrm{EE}\left(\mathbf{w}_n, \rho_n, \mathbf{\Theta}, \mathbf{z}\right) \tag{20a}$$

$$\text{s.t. } P_T \le P_{\mathrm{Max}}, \tag{20b}$$

$$\gamma_n^{(\mathrm{DDR})}\left(\mathbf{w}_n, \rho_n, \mathbf{\Theta}, \mathbf{z}\right) \ge 2^{R_n^{(\mathrm{D})}} - 1, \forall n, \tag{20c}$$

$$P_{\mathrm{EH},n}^{(\mathrm{DDR})}\left(\mathbf{w}_n, \rho_n, \mathbf{\Theta}, \mathbf{z}\right) \ge \mathcal{F}_n(P_{\mathrm{DC},n}^{(\mathrm{DDR})}), \forall n, \tag{20d}$$

$$P_{\mathrm{EH},l}^{(\mathrm{EHR})}\left(\mathbf{w}_n, \mathbf{\Theta}, \mathbf{z}\right) \ge \mathcal{F}_l(P_{\mathrm{DC},l}^{(\mathrm{EHR})}), \forall l, \tag{20e}$$

$$\gamma_{l,n}^{(\mathrm{EHR})}\left(\mathbf{w}_n, \mathbf{\Theta}, \mathbf{z}\right) \le 2^{R_l^{(\mathrm{E})}} - 1, \forall l, n, \tag{20f}$$

$$0 < \rho_n < 1, \forall n, \tag{20g}$$

$$\left|\mathbf{\Theta}_{[q,q]}\right| \le 1, \forall q. \tag{20h}$$

In problem $\mathbf{P}_0$, (20a) is the fractional objective for EE maximization. Furthermore, the power budget is presented as (20b), where P_{Max} is the maximum transmitting power. In addition, (20c) and (20d) denote the ID and EH requirements of the DDR, respectively. As for them, $R_n^{(\mathrm{D})}$ and $P_{\mathrm{DC},n}^{(\mathrm{DDR})}$ are the performance thresholds. The $\mathcal{F}_n(P_{\mathrm{DC},n}^{(\mathrm{DDR})})$ denote the inverse form of expression (15), which is presented as

$$\mathcal{F}_n(P_{\mathrm{DC},n}^{(\mathrm{DDR})}) = \varpi_n - \frac{1}{\kappa_n}\ln\left(\frac{\upsilon_{B,n}\left(1+\chi_n\right)}{P_{\mathrm{DC},n}^{(\mathrm{DDR})}\chi_n + \upsilon_{B,n}} - 1\right), \tag{21}$$

Algorithm 1. *The proposed alternative optimization strategy*

Input: $\varepsilon_{\mathrm{AO}}$, $\mathbf{\Theta}^{(0)}$;
1: Set $i = 1$, D_{AO}, $\mathrm{EE}^{(0)} = 0$;
2: **while** $D_{\mathrm{AO}} \ge \varepsilon_{\mathrm{AO}}$ **do**
3: Resolving the subproblem relying on the variables $\left\{\mathbf{w}_n^{(i)}, \rho_n^{(i)}, \mathbf{z}^{(i)}\right\}$ with the optimal $\mathbf{\Theta}^{*(i-1)}$;
4: Resolving the subproblem relying on $\mathbf{\Theta}^{(i)}$ with the optimal variables $\left\{\mathbf{w}_n^{*(i)}, \rho_n^{*(i)}, \mathbf{z}^{*(i)}\right\}$;
5: Set $D_{\mathrm{AO}} = \mathrm{EE}^{(i)} - \mathrm{EE}^{(i-1)}$;
6: Update $i = i + 1$;
7: **end while**
Output: $\left\{\mathbf{w}_n^{*(i)}, \rho_n^{*(i)}, \mathbf{z}^{*(i)}, \mathbf{\Theta}^{*(i)}\right\}$

Similarly, the power demand for EHR is written as (20e). For ensuring network security, the constraint (20f) is introduced to restrict unauthorized demodulation of EHR. In particular, its SINR must be controlled less than $(2^{R_l^{(\mathrm{E})}} - 1)$. Moreover, (20g) is the configuration range of the PS ratio. Besides, (20h) is the physical restriction of the load reflection coefficients. $\mathbf{P}_0$ is a non-convex problem with coupled variables. Additionally, the introduced practical communication model (9) causes it more intractable. In the next section, the effective solution strategy will be presented.

IV. THE OPTIMIZATION STRATEGY

To tackle the proposed problem, we first need to decouple the variables. Particularly, the active beamforming vector $\mathbf{w}_n$, PS ratio ρ_n, and artificial noise vector $\mathbf{z}$ consist of a subproblem. Moreover, another subproblem is based on the reflection coefficients of the $\mathbf{\Theta}$. These two subproblems will be solved iteratively until the final convergence condition is met. This scheme can be found in the Algorithm 1.

4.1 Solution for $\left\{\mathbf{w}_n^{(i)}, \boldsymbol{\rho}_n^{(i)}, \mathbf{z}^{(i)}\right\}$

The first subproblem is still non-convex, which should be further transformed. Particularly, the SDR approach is applied to the variables $\mathbf{w}_n^{(i)}$ and $\mathbf{z}^{(i)}$ as $\mathbf{W}_n^{(i)} = \mathbf{w}_n^{(i)}\mathbf{w}_n^{(i)^H}$ and $\mathbf{Z}^{(i)} = \mathbf{z}^{(i)}\mathbf{z}^{(i)^H}$ with $\mathbf{W}_n^{(i)} \succeq 0$, $\mathrm{rank}(\mathbf{W}_n^{(i)}) = 1$, $\mathbf{Z}^{(i)} \succeq 0$, and $\mathrm{rank}(\mathbf{Z}^{(i)}) = 1$. Besides, we can define $\mathbf{H_n}^{(i)} = \mathbf{h_n}^{(i)^H}\mathbf{h_n}^{(i)}$ with the fixed $\mathbf{\Theta}^{*(i-1)}$. As examples, the EH power and SINR

$$\mathbf{P}_{\text{1-1}}: \max_{\left\{\mathbf{W}_n^{(i)},\mathbf{Z}^{(i)},\rho_n^{(i)}\right\}} \text{EE}\left(\mathbf{W}_n^{(i)},\mathbf{Z}^{(i)},\rho_n^{(i)}\right) \tag{24a}$$

$$\text{s.t. Tr}\left(\sum_{n=1}^{N_D}\mathbf{W}_n^{(i)}+\mathbf{Z}^{(i)}\right)\le P_{\text{Max}}, \tag{24b}$$

$$\frac{\text{Tr}\left(\mathbf{H}_n^{(i)}\mathbf{W}_n^{(i)}\right)}{2^{R_n^{(\text{D})}}-1}\ge \text{Tr}\left(\mathbf{H}_n^{(i)}\left(\sum_{k\neq n}^{N_D}\mathbf{W}_k^{(i)}+\mathbf{Z}^{(i)}\right)\right)+\sigma_n^2+\frac{\delta_n^2}{\rho_n^{(i)}},\forall n, \tag{24c}$$

$$\text{Tr}\left(\mathbf{H}_n^{(i)}\left(\sum_{n=1}^{N_D}\mathbf{W}_n^{(i)}+\mathbf{Z}^{(i)}\right)\right)\ge\frac{\mathcal{F}_n(P_{\text{DC},n}^{(\text{DDR})})}{(1-\rho_n^{(i)})},\forall n, \tag{24d}$$

$$\text{Tr}\left(\mathbf{H}_n^{(i)}\left(\sum_{n=1}^{N_D}\mathbf{W}_n^{(i)}+\mathbf{Z}^{(i)}\right)\right)\ge\mathcal{F}_l(P_{\text{DC},l}^{(\text{EHR})}),\forall l, \tag{24e}$$

$$\frac{\text{Tr}\left(\mathbf{H}_l^{(i)}\mathbf{W}_n^{(i)}\right)}{2^{R_l^{(\text{E})}}-1}\le \text{Tr}\left(\mathbf{H}_l^{(i)}\left(\sum_{k\neq l}^{N_D}\mathbf{W}_k^{(i)}+\mathbf{Z}^{(i)}\right)\right)+\sigma_l^2+\delta_l^2,\forall l,n, \tag{24f}$$

$$0<\rho_n^{(i)}<1,\forall n, \tag{24g}$$

$$\mathbf{W}_n^{(i)}\succeq 0,\text{rank}(\mathbf{W}_n^{(i)})=1,\mathbf{Z}^{(i)}\succeq 0,\text{rank}(\mathbf{Z}^{(i)})=1. \tag{24h}$$

of the DDR can be rewritten as

$$\begin{aligned}&P_{\text{EH},n}^{(\text{DDR})}\left(\mathbf{W}_n^{(i)},\mathbf{Z}^{(i)},\rho_n^{(i)}\right)\\&=(1-\rho_n^{(i)})\text{Tr}\left(\mathbf{H}_n^{(i)}\left(\sum_{n=1}^{N_D}\mathbf{W}_n^{(i)}+\mathbf{Z}^{(i)}\right)\right),\end{aligned} \tag{22}$$

$$\begin{aligned}&\gamma_n^{(\text{DDR})}\left(\mathbf{W}_n^{(i)},\mathbf{Z}^{(i)},\rho_n^{(i)}\right)\\&=\frac{\text{Tr}\left(\mathbf{H}_n^{(i)}\mathbf{W}_n^{(i)}\right)}{\text{Tr}\left(\mathbf{H}_n^{(i)}\left(\sum_{k\neq n}^{N_D}\mathbf{W}_k^{(i)}+\mathbf{Z}^{(i)}\right)\right)+\sigma_n^2+\frac{\delta_n^2}{\rho_n^{(i)}}}.\end{aligned} \tag{23}$$

Similarly, the subproblem with SDR can be presented as $\mathbf{P}_{\text{1-1}}$, where the left-hand side of (24b) is the P_T.

Although all the constraints are convex except (24h), the objective (24a) remains the fractional form. To further resolve it, we introduce extra constraints as

$$\mathbf{P}_{\text{1-2}}: \max_{\left\{\begin{smallmatrix}\mathbf{w}_n^{(i)},\rho_n^{(i)},\\ \mathbf{z}^{(i)},\varrho_n^{(i)}\end{smallmatrix}\right\}} \frac{\sum_{n=1}^{N_D}g_n^{(i)}}{P_T+P_B+\epsilon\left(\sum_{n=1}^{N_D}g_n^{(i)}\right)} \tag{25a}$$

$$\text{s.t. Tr}(\hat{\mathbf{H}}_n^{(i)}\mathbf{W}_n^{(i)})\ge\exp(u_n^{(i)}+v_n^{(i)}),\forall n, \tag{25b}$$

$$\exp(u_n^{(i)})\ge 2^{(g_n^{(i)})}-1,\forall n, \tag{25c}$$

$$\text{Tr}\left(\mathbf{H}_n^{(i)}\left(\sum_{k\neq n}^{N_D}\mathbf{W}_k^{(i)}+\mathbf{Z}^{(i)}\right)\right)+\sigma_n^2+\frac{\delta_n^2}{\rho_n^{(i)}}\le\exp(v_n^{(i)}),\forall n, \tag{25d}$$

(24b)-(24h).

where $\varrho_n^{(i)}=\{g_n^{(i)},u_n^{(i)},v_n^{(i)}\}$. So far, the objective (25a) of $\mathbf{P}_{\text{1-2}}$ has satisfied the form of Dinkelbach's algorithm.

Lemma 1. *Under the condition that ξ^* is unique zero, (25a) can be further transformed into a subtractive expression as*

$$\begin{aligned}&\Omega\left(\mathbf{W}_n^{(j)},\mathbf{Z}^{(i)},g_n^{(i)}\right)\\&=\sum_{n=1}^{N_U}g_n^{(i)}-\xi^*\left(P_T+P_B+\epsilon\left(\sum_{n=1}^{N_D}g_n^{(i)}\right)\right).\end{aligned} \tag{26}$$

Proof. The detailed proof process has been written in [21], hence we do not describe it further.

$$\mathbf{h}_n^{(i)}(\hat{\theta}_j^{(i)}) = \mathbf{s}_{RT,n} + \mathbf{s}_{RI,n}(-\mathbf{S}_{II} + \mathbf{Q}_j^{(i)} + \hat{\theta}_j^{(i)}\mathbf{g}_j\mathbf{g}_j^T)^{-1}\mathbf{S}_{IT,n}, \tag{30}$$

$$(-\mathbf{S}_{II} + \mathbf{Q}_j^{(i)} + \hat{\theta}_j^{(i)}\mathbf{g}_j\mathbf{g}_j^T)^{-1} = \left(\left(-\mathbf{S}_{II} + \mathbf{Q}_j^{(i)}\right)^{-1} - \frac{\left(-\mathbf{S}_{II} + \mathbf{Q}_j^{(i)}\right)^{-1}\mathbf{g}_j\mathbf{g}_j^T\left(-\mathbf{S}_{II} + \mathbf{Q}_j^{(i)}\right)^{-1}}{\frac{1}{\hat{\theta}_j^{(i)}} + \mathbf{g}_j^T\left(-\mathbf{S}_{II} + \mathbf{Q}_j^{(i)}\right)^{-1}\mathbf{g}_j}\right), \tag{31}$$

When adopting the Dinkelbach's algorithm, ξ^* in (26) should be generated from the iterative solution for $\mathbf{P}_{1\text{-}2}$. With (26), the fractional objective turns out to be the solvable form. However, the introduced (25c) and (25d) still contain exponential terms, which makes the $\mathbf{P}_{1\text{-}2}$ tough to resolve. Therefore, the SCA scheme is adopted to linearize them. Particularly, we can achieve the lower bound for the $\exp(u_n^{(i)})$ and $\exp(v_n^{(i)})$ as

$$\exp(u_n^{(i)}) \geq \exp(\dot{u}_n^{(i)}) + \exp(\dot{u}_n^{(i)})(\dot{u}_n^{(i)} - u_n^{(i)}), \tag{27}$$

$$\exp(v_n^{(i)}) \geq \exp(\dot{v}_n^{(i)}) + \exp(\dot{v}_n^{(i)})(\dot{v}_n^{(i)} - v_n^{(i)}), \tag{28}$$

where $\dot{u}_n^{(i)}$ and $\dot{v}_n^{(i)}$ are the feasible values, which will be updated after each iteration of SCA. After replacing the (25c) and (25d), the problem $\mathbf{P}_{1\text{-}2}$ becomes

$$\begin{aligned}
\mathbf{P}_{1\text{-}3}: \max_{\left\{\begin{smallmatrix}\mathbf{w}_n^{(i)},\rho_n^{(i)},\\ \mathbf{z}^{(i)},\varrho_n^{(i)}\end{smallmatrix}\right\}} \ & \Omega\left(\mathbf{W}_n^{(i)}, \mathbf{Z}^{(i)}, g_n^{(i)}\right) \\
& \exp(\dot{u}_n^{(i)}) + \exp(\dot{u}_n^{(i)})(\dot{u}_n^{(i)} - u_n^{(i)}) \\
& \geq 2^{(u_n^{(i)})} - 1, \forall n, \qquad (29a) \\
& \mathrm{Tr}\left(\mathbf{H}_n^{(i)}\left(\sum_{k\neq n}^{N_D}\mathbf{W}_k^{(i)} + \mathbf{Z}^{(i)}\right)\right) + \sigma_n^2 + \frac{\delta_n^2}{\rho_n^{(i)}} \\
& \leq \exp(\dot{v}_n^{(i)}) + \exp(\dot{v}_n^{(i)})(\dot{v}_n^{(i)} - v_n^{(i)}), \forall n, \qquad (29b) \\
& (24b)\text{-}(24h), (25b).
\end{aligned}$$

where we omit iterative notations of Dinkelbach's algorithm and SCA scheme for expression simplicity. When the rank-one constraint in $\mathbf{P}_{1\text{-}3}$ is ignored, the problem turn to a convex problem. Moreover, the recovery approach satisfying the rank constraint and the whole solution strategy are presented in Algorithm 2.

Algorithm 2. *The Dinkelbach's algorithm based on the SCA approach.*

Input: $\varepsilon_{\text{DK}}, \varepsilon_{\text{SCA}}$;
1: Set D_{DK}, ξ^*;
2: **while** $D_{\text{DK}} \geq \varepsilon_{\text{DK}}$ **do**
3: Set $\dot{u}_n^{(i)}, \dot{v}_n^{(i)}, D_{\text{SCA}}$;
4: **while** $D_{\text{SCA}} \geq \varepsilon_{\text{SCA}}$ **do**
5: Resolve the problem $\mathbf{P}_{1\text{-}3}$ to achieve the optimal variables;
6: Update feasible values of SCA;
7: Set D_{SCA} with the difference between this and the previous iteration of EE
8: **end while**
9: Update $\xi^* = \text{EE}\left(\mathbf{W}_n^{*(i)}, \mathbf{Z}^{*(i)}, \rho_n^{*(i)}\right)$;
10: Set D_{DK} with the difference between this and the previous iteration of (26).
11: **end while**
12: Achieve the vectors $\mathbf{w}_n^{*(i)}$ and $\mathbf{z}^{*(i)}$ with the Gaussian randomization or eigen decomposition [21]
Output: $\left\{\mathbf{w}_n^{*(i)}, \rho_n^{*(i)}, \mathbf{z}^{*(i)}\right\}$

4.2 Solution for $\boldsymbol{\Theta}^{(i)}$

The situation for the subproblem of $\boldsymbol{\Theta}^{(i)}$ is more intractable, on account of the inner and the outer inverse of the utilized model (9). We propose a novel element-wise block coordinate descent (BCD) method to tackle it. In particular, the Sherman-Morrison transformation [22] is introduced to decompose the model (9).

First, (9) can be written as its equivalent form (30). In the equation, $\hat{\theta}_j^{(i)}$ can be achieve as $\hat{\theta}_j^{(i)} = \boldsymbol{\Theta}_{[j,j]}^{(i)^{-1}}$. Moreover, $\mathbf{Q}_j^{(i)}$ is the matrix $\boldsymbol{\Theta}^{(i)^{-1}}$ with the $\boldsymbol{\Theta}_{[j,j]}^{(i)^{-1}} = 0$. Besides, the $\mathbf{g}_j$ is the $N_I \times 1$ vector with all zero elements except that the j^{th} element is one. With (30), the Sherman-Morrison formula can be applied to replace the inverse term as in (31). When $\mathbf{Q}_j^{(i)}$ is treated

$$\mathbf{P}_{2\text{-}1}: \max_{\left\{\hat{\mathbf{C}}_j^{(i)}\right\}} \mathrm{EE}\left(\mathbf{C}_j^{(i)}\right) \tag{36a}$$

$$\frac{\mathrm{Tr}\left(\mathbf{E}_{n,j}^{(i)}\hat{\mathbf{C}}_j^{(i)}\mathbf{W}_n^{*(i)}\right)}{2^{R_n^{(\mathrm{D})}}-1} \geq \mathrm{Tr}\left(\mathbf{E}_{n,j}^{(i)}\hat{\mathbf{C}}_j^{(i)}\left(\sum_{k\neq n}^{N_D}\mathbf{W}_k^{*(i)}+\mathbf{Z}^{*(i)}\right)\right)+\sigma_n^2+\frac{\delta_n^2}{\rho_n^{*(i)}}, \forall n, \tag{36b}$$

$$\mathrm{Tr}\left(\mathbf{E}_{n,j}^{(i)}\hat{\mathbf{C}}_j^{(i)}\left(\sum_{n=1}^{N_D}\mathbf{W}_n^{*(i)}+\mathbf{Z}^{*(i)}\right)\right) \geq \frac{\mathcal{F}_n(P_{\mathrm{DC},n}^{(\mathrm{DDR})})}{(1-\rho_n^{*(i)})}, \forall n, \tag{36c}$$

$$\mathrm{Tr}\left(\mathbf{E}_{l,j}^{(i)}\hat{\mathbf{C}}_j^{(i)}\left(\sum_{n=1}^{N_D}\mathbf{W}_n^{*(i)}+\mathbf{Z}^{*(i)}\right)\right) \geq \mathcal{F}_l(P_{\mathrm{DC},l}^{(\mathrm{EHR})}), \forall l, \tag{36d}$$

$$\frac{\mathrm{Tr}\left(\mathbf{E}_{l,j}^{(i)}\hat{\mathbf{C}}_j^{(i)}\mathbf{W}_l^{*(i)}\right)}{2^{R_l^{(\mathrm{E})}}-1} \leq \mathrm{Tr}\left(\mathbf{E}_{l,j}^{(i)}\hat{\mathbf{C}}_j^{(i)}\left(\sum_{k\neq l}^{N_D}\mathbf{W}_k^{*(i)}+\mathbf{Z}^{*(i)}\right)\right)+\sigma_l^2+\delta_l^2, \forall l, n, \tag{36e}$$

$$1-t_j^{(i)}\hat{\mathbf{C}}_{j,[2,1]}^{(i)}-t_j^{(i)^H}\hat{\mathbf{C}}_{j,[1,2]}^{(i)}+t_j^{(i)}t_j^{(i)^H}\hat{\mathbf{C}}_{j,[1,1]}^{(i)} \leq \hat{\mathbf{C}}_{j,[1,1]}^{(i)}, \tag{36f}$$

$$\hat{\mathbf{C}}_{j,[2,2]}^{(i)}=1, \hat{\mathbf{C}}_j^{(i)} \succeq 0, \mathrm{rank}(\hat{\mathbf{C}}_j^{(i)})=1. \tag{36g}$$

Algorithm 3. *The BCD scheme for the subproblem of* $\mathbf{\Theta}^{(0)}$

Input: $\varepsilon_{\mathrm{BCD}}$, $\mathbf{\Theta}^{(0)}$;

1: Set D_{BCD}, $\mathrm{EE}^{(0)}=0$;
2: **while** $D_{\mathrm{BCD}} \geq \varepsilon_{\mathrm{BCD}}$ **do**
3: **for** $j=1:N_I$ **do**
4: Resolve the problem $\mathbf{P}_{2\text{-}2}$ with the Dinkelbach's algorithm and SCA scheme;
5: Update $\mathbf{\Theta}_{[j,j]}^{*(i)^{-1}}=\hat{\theta}_j^{*(i)}$;
6: **end for**
7: Set $j=1$;
8: Update the value D_{BCD} with the optimal EE in this iteration and EE from the previous iteration;
9: **end while**

Output: $\left\{\mathbf{\Theta}^{*(i)}\right\}$

as the given matrix, the remaining variable is $\hat{\theta}_j^{(i)}$. So far, the double-layer inverse in (9) has been turned into a more solvable form. Based on the above transformation, we can optimize the elements of $\mathbf{\Theta}^{(i)}$ one by one. The specific idea of the BCD can be found in Algorithm 3. During solving j^{th} element, a new variable can be defined as

$$c_j^{(i)}=\frac{1}{\hat{\theta}_j^{(i)}}+\mathbf{g}_j^T\left(-\mathbf{S}_{II}+\mathbf{Q}_j^{(i)}\right)^{-1}\mathbf{g}_j, \tag{32}$$

Then, the end-to-end model can be reformed as the following equation.

$$\mathbf{h}_n^{(i)}(c_j^{(i)})=\mathbf{f}_{n,j}^{(i)}+c_j^{(i)}\mathbf{m}_{n,j}^{(i)}, \tag{33}$$

where the shorthand notations represent

$$\mathbf{f}_{n,j}^{(i)}=\mathbf{s}_{RT,n}+\mathbf{s}_{RI,n}(-\mathbf{S}_{II}+\mathbf{Q}_j^{(i)})^{-1}\mathbf{S}_{IT,n}, \tag{34}$$

$$\begin{aligned}\mathbf{m}_{n,j}^{(i)}=&-\mathbf{s}_{RI,n}((-\mathbf{S}_{II}+\mathbf{Q}_j^{(i)})^{-1}\mathbf{g}_j\\&\times\mathbf{g}_j^T(-\mathbf{S}_{II}+\mathbf{Q}_j^{(i)})^{-1})\mathbf{S}_{IT,n}.\end{aligned} \tag{35}$$

As for (33), we can reform $\mathbf{h}_n^{(i)}(\hat{\mathbf{c}}_j^{(i)})=\hat{\mathbf{c}}_j^{(i)}\mathbf{e}_{n,j}^{(i)}$, where $\hat{\mathbf{c}}_j^{(i)}=[c_j^{(i)},1]$ and $\mathbf{e}_{n,j}^{(i)}=[\mathbf{m}_{n,j}^{(i)};\mathbf{f}_{n,j}^{(i)}]$. Further, the SDR approach can be adopted again. In particular, the $\hat{\mathbf{C}}_j^{(i)}=\hat{\mathbf{c}}_j^{(i)^H}\hat{\mathbf{c}}_j^{(i)}$ with the constraints $\hat{\mathbf{C}}_j^{(i)}\succeq 0$, and $\mathrm{rank}(\hat{\mathbf{C}}_j^{(i)})=1$ is introduced. Similarly, $\mathbf{E}_{n,j}^{(i)}=\mathbf{e}^{(i)}{}_{n,j}\mathbf{e}_{n,j}^{(i)^H}$. With the SDR, we can present the subproblem for $\mathbf{\Theta}^{(i)}$ as in $\mathbf{P}_{2\text{-}1}$. As for the constraint (36f), $t_j^{(i)}=\mathbf{g}_j^T(\mathbf{S}_{II}+\mathbf{Q}_j^{(i)})^{-1}\mathbf{g}_j$. Moreover, it comes from the equivalent inequality as

$$\left(c_j^{(i)}-t_j^{(i)}\right)\left(c_j^{(i)}-t_j^{(i)}\right)^H \leq 1, \tag{36}$$

$$\mathbf{P}_{2\text{-}2}: \max_{\left\{\hat{\mathbf{C}}_j^{(i)}, \chi_{n,j}^{(i)}\right\}} \sum_{n=1}^{N_U} o_{n,j}^{(i)} - \xi^* \left(P_T + P_B + \epsilon \left(\sum_{n=1}^{N_D} o_{n,j}^{(i)} \right) \right) \tag{37a}$$

$$\text{s.t. } \mathrm{Tr}\left(\mathbf{E}_{n,j}^{(i)} \hat{\mathbf{C}}_j^{(i)} \mathbf{W}_n^{*(i)}\right) \geq \exp(\zeta_{n,j}^{(i)} + \nu_{n,j}^{(i)}), \forall n, \tag{37b}$$

$$\exp(\dot{\zeta}_{n,j}^{(i)}) + \exp(\dot{\zeta}_{n,j}^{(i)})(\dot{\zeta}_{n,j}^{(i)} - \zeta_{n,j}^{(i)}) \geq 2^{(o_{n,j}^{(i)})} - 1, \forall n, \tag{37c}$$

$$\mathrm{Tr}\left(\mathbf{E}_{n,j}^{(i)} \hat{\mathbf{C}}_j^{(i)} \left(\sum_{k \neq n}^{N_D} \mathbf{W}_k^{*(i)} + \mathbf{Z}^{*(i)} \right) \right) + \sigma_n^2 + \frac{\delta_n^2}{\rho^{*(i)}} \leq \exp(\dot{\nu}_{n,j}^{(i)}) + \exp(\dot{\nu}_{n,j}^{(i)})(\dot{\nu}_{n,j}^{(i)} - \nu_{n,j}^{(i)}), \forall n, \tag{37d}$$

(36b)-(36g).

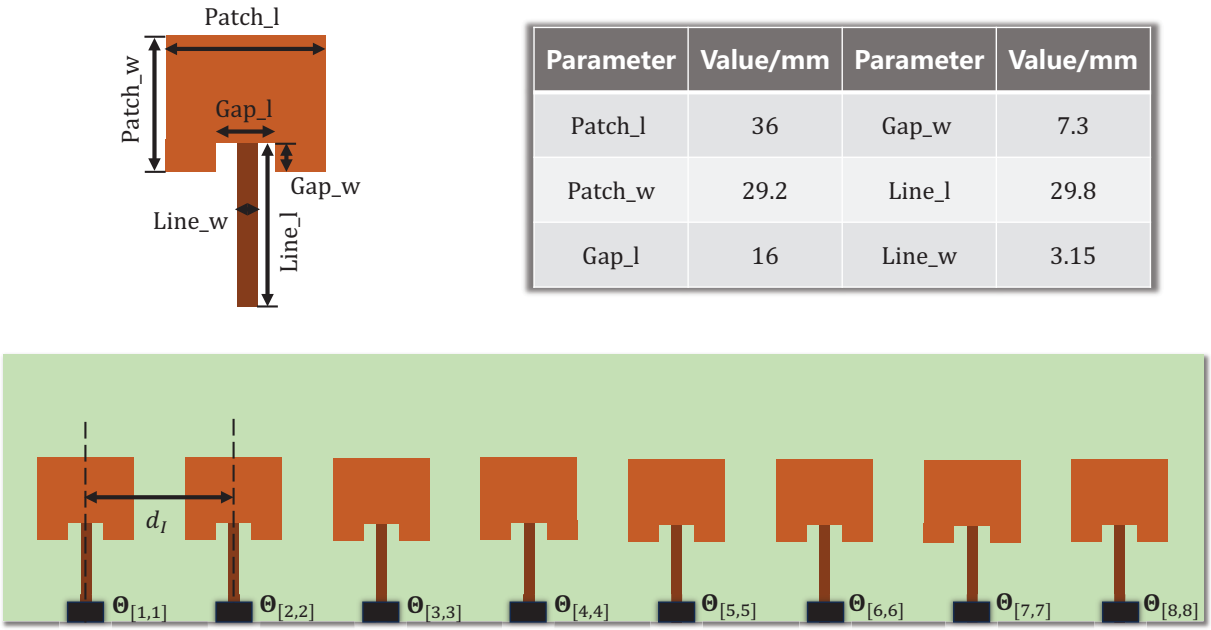

Parameter	Value/mm	Parameter	Value/mm
Patch_l	36	Gap_w	7.3
Patch_w	29.2	Line_l	29.8
Gap_l	16	Line_w	3.15

Figure 2. *The RIS design and relevant parameters.*

which generated from (20h) for representing the physical restriction of the reflection coefficient. Further, the solution approach for $\mathbf{P}_{2\text{-}1}$, which is similar to the last subsection, can be introduced to construct a solvable problem. Particularly, the strategy also relies on Dinkelbach's algorithm and SCA approach, thus we no longer present the details and only show the transformed problem as in the problem $\mathbf{P}_{2\text{-}2}$, where $\chi_{n,j}^{(i)} = \{o_{n,j}^{(i)}, \zeta_{n,j}^{(i)}, \nu_{n,j}^{(i)}\}$. When the rank-constraint of (36g) is omitted, the problem is a convex problem. Moreover, the similar recovery way from $\mathbf{C}_j^{*(i)}$ to $\hat{\theta}_j^{*(i)}$, which satisfies the rank-one constraint, can be found in Algorithm 2.

The description of the whole solution scheme has been finished. It is worth mentioning that the subproblem $\mathbf{P}_{2\text{-}1}$ can be simplified when the self S-parameter $\mathbf{S}_{II} = \mathbf{0}$. However, it may be ideal and bring a non-negligible optimization deviation. This fact will be shown in the next section.

V. SIMULATION RESULTS

5.1 RIS Design and S-parameter Extraction

The hardware characteristics of RIS are included in the S-parameter. For revealing its influence on the

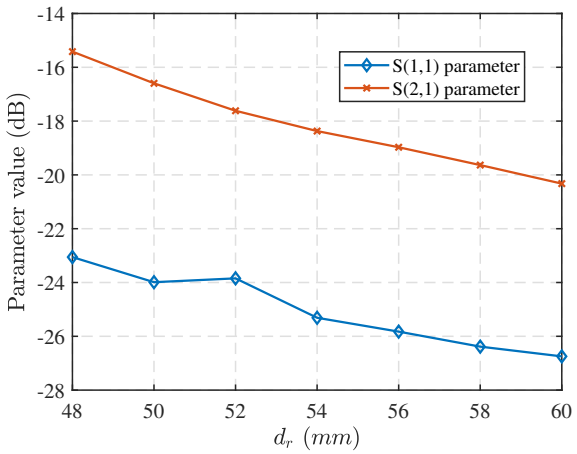

Figure 3. *The S-parameters of the proposed RIS.*

network, we first need to extract the parameter. Particularly, a linear-array RIS in Figure 2 is designed through the software of EM analysis (Ansys Electronics 2022). In detail, it consists of 8 elements with the patch form, which is mostly adopted in the RIS design. Moreover, the patch mainly includes the rectangular radiation part and the transmission line. The end of the line can be connected by the component such as a varactor to achieve controllability. Indeed, the variable $\mathbf{\Theta}$ just relies on this. Moreover, all the parameters are described in Figure 2. Further, we present the impacts of the element spacing d_r on the S-parameters as in Figure 3. Particularly, we select S(1,1) and S(2,1) values to show the mismatching and MC effect of RIS, respectively. It can be seen that they all decrease when the d_r increases. It means that the larger element spacings indeed bring better matching conditions and lower MC. In the next subsection, these effects will be analyzed from the perspective of the network.

5.2 Numerical Results

With the S-parameter extracted from a practical RIS, we then conduct research about the EE performance of the RIS-assisted SWIPT network. Specifically, the results are presented to show the significance of the hardware characteristics. In particular, we will analyze the distinct effects of network settings on the network EE. What's more, the influences from RIS configurations will also be considered. The scenario is simplified as 2-dimension, where the Tx array is set at $(0m,0m)$, the RIS is positioned at $(1m,1m)$, and the receivers (two DDRs and one EHR) are generated from a zone with $(2m,\text{-}4m)$ center and $3m$ radius. Besides, the whole network operates at 2.45GHz.

In this paper, the transmission parameters in (9) are the Rician channels as the similar setting in [19]. Particularly, they have the form as

$$\mathbf{S}_{AB} = \sqrt{L_{AB}}\left(\sqrt{\frac{\mathcal{K}}{1+\mathcal{K}}}\mathbf{H}_{AB}^{\text{LoS}} + \sqrt{\frac{1}{1+\mathcal{K}}}\mathbf{H}_{AB}^{\text{NLoS}}\right). \tag{38}$$

where $AB \in \{RT, RI, IT\}$. The Rician factor is presented as $\mathcal{K} = 10$dB. Moreover, the pathloss component is written as $L_{AB} = (\frac{\lambda}{4\pi})^2 \left(\frac{d_{AB}}{D_0}\right)^{-\alpha_{AB}}$, in which the reference distance is set as $D_0 = 1m$. Further, the pathloss factors are $\alpha_{RT} = 3$, $\alpha_{IT} = 2.2$, and $\alpha_{RI} = 2.2$ for all the receivers.

Regarding the default simulation settings, the maximum transmitting power is $P_{\text{Max}} = 8$W, the ID demand of the DDR is $R_n^{(\text{D})} = 3$bit/s/Hz, $\forall n$, the maximum rate of the potential eavesdropper is $R_l^{(\text{E})} = 1$bits/s/Hz, $\forall l$, and the minimal EH power for all the DDRs and the EHR is $P_{\text{DC}}^{(\text{D})} = 1.3\mu$W. Moreover, the $P_c = 1$W, $P_I = 0.01$W, $\epsilon = 0.01$ are the power-dissipation values of the hardware components and the ratio of rate-dependent power consumption. The noise power levels for all the receivers are $\sigma^2 = -100$dBm and $\delta^2 = -80$dBm. In addition, the circuit parameters for all the rectifying circuits are $\varpi = 5.61$, $\kappa = 0.242$, and $v_B = 8.577$.

5.2.1 Convergence Behaviors

The proposed algorithm is mainly based on the outer-layer alternative strategy in Algorithm 1 and the inner-layer BCD scheme in Algorithm 3. To further show their effectiveness, we present the convergence behaviors in Figure 4a and 4b, respectively. As for Figure 4a, each point represents the EE value after optimizing all the RIS elements in one iteration of the BCD scheme. With a couple of iterations, the EE smoothly converges to a stable value. Moreover, there are only a few steps for achieving the final convergence of Algorithm 3 in Figure 4b. Particularly, the convergence behaviors of distinct simulation settings are similar. These results further demonstrate the performance of the proposed optimization schemes. Indeed, the BCD scheme can be simplified with $\mathbf{S}_{II} = \mathbf{0}$, which is the ideal case.

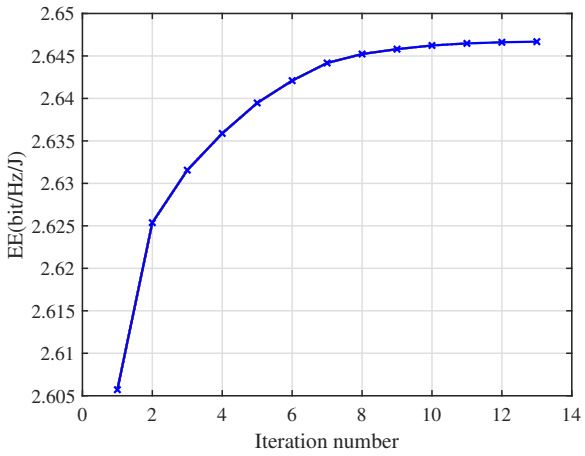

(a) *The convergence behavior of Algorithm 3.*

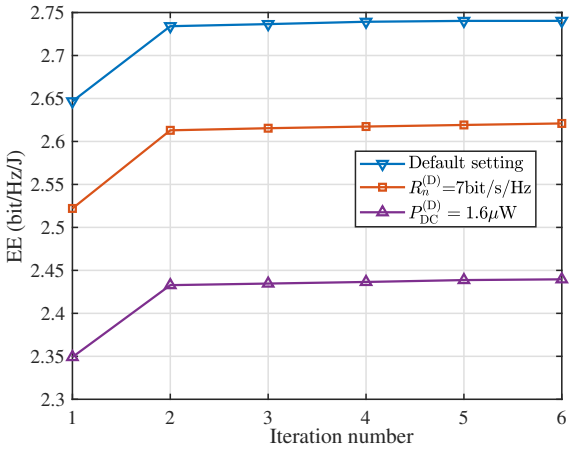

(b) *The convergence behavior of Algorithm 1.*

Figure 4. *The convergence behaviors of the proposed algorithms*

Nevertheless, the resulting loss of performance may not be neglectable.

5.2.2 The Effect of Rate Demand $R_n^{(\mathrm{D})}$ on EE

The influences brought from the distinct rate demand $R_n^{(\mathrm{D})}$ are presented in this subsection. In detail, the hardware effects (HE), including the matching effect and the MC effect, are analyzed thoroughly. As shown in Figure 5, the HE awareness (HEA) represents the results optimized from practical cases considering these effects, namely, $\mathbf{S}_{II} \neq \mathbf{0}$. On the contrary, HE unawareness (HEU) means that the optimized variables from ideal cases, $\mathbf{S}_{II} = \mathbf{0}$, are deployed in practical situations. It is apparent that the HEA results perform better than HEU results in the

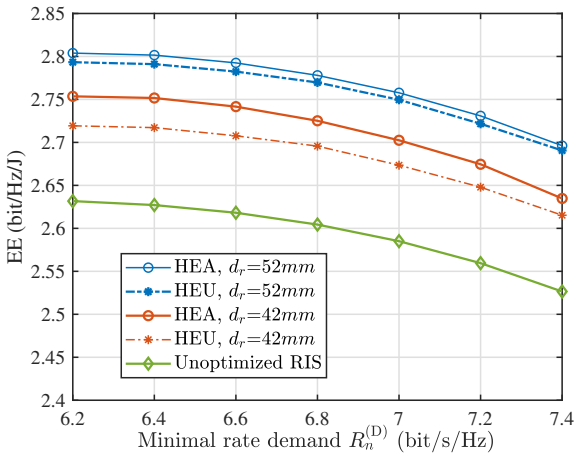

Figure 5. *The effect of rate demand $R_n^{(\mathrm{D})}$ on EE.*

settings with two distinct RIS element spacings d_r. Moreover, these performance gaps in $d_r = 42mm$ are larger than those in $d_r = 52mm$, since the mismatching and strong MC effects are prominent in the more compact RIS. Figure 3 already has shown these influences at the end level. Furthermore, the HEA and HEU results from $d_r = 52mm$ are better than those in $d_r = 42mm$ due to the larger physical space. With the above phenomena, there should be careful trade-offs between the network performance and the RIS configurations. Although the EE levels of these cases are different, they all outperform the unoptimized RIS situation, which proves the crucial role of RIS in the SWIPT network. In addition, these results have similar descending trends with the increased minimal rate demand of the DDR. The reason is that more energy should be distributed to the DDR with poor channel conditions, which causes less enhancement space for the better-channel DDR. Then the worse sum rate term of the EE occurs naturally. Besides, the increasing rate-dependent power dissipation also will pull down EE levels.

5.2.3 The Effect of Power Requirement $P_{\mathrm{DC}}^{(\mathrm{D})}$ on EE

The power requirement $P_{\mathrm{DC}}^{(\mathrm{D})}$, which is strongly related to the power dissipation of the network, also impacts the EE performance. The specific simulation results are shown in Figure 6. The comparative cases are set as in Figure 5. Moreover, the HEA results still have better EE performance. As the similar reasons stated in the last subsection, we omit the detailed explana-

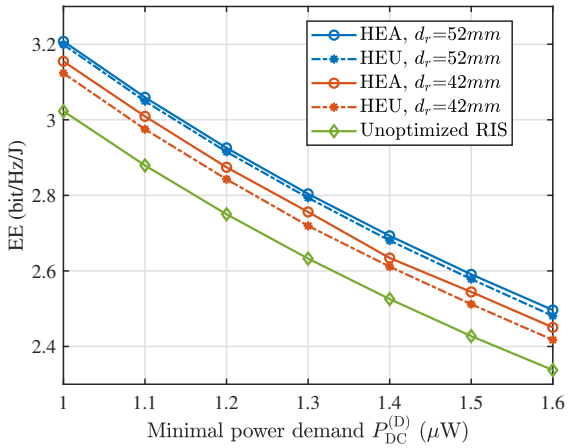

Figure 6. *The effect of power requirement $P_{\mathrm{DC}}^{(\mathrm{D})}$ on EE.*

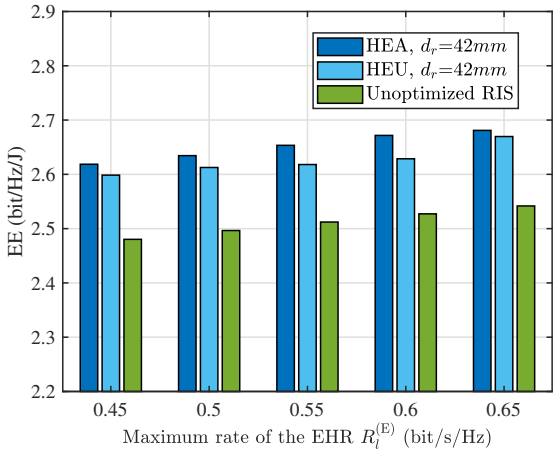

Figure 7. *The effect of EHR maximum rate $R_l^{(\mathrm{E})}$ on EE.*

tion here. In all cases, the decreasing tendencies of EE come from the continuous input of power resources to satisfy the increasing power requirements $P_{\mathrm{DC}}^{(\mathrm{D})}$. This conclusion supports the idea that the low-power receiver design should be critical for high EE targets.

5.2.4 The Effect of EHR Maximum Rate $R_l^{(\mathrm{E})}$ on EE

In this paper, the EHR, which may try to decode the unauthorized information from the DDR, exists as the potential eavesdropper. Considering the network security, the maximum rate of EHR should be constrained as low as possible. We study the network EE under the distinct maximum rates of the EHR as in Figure 7. For clarity of presentation, we only show the cases of $d_r = 42mm$ and the situation of unoptimized RIS. Particularly, the HEA still maintains its advantage over the other cases. In addition, we can find that all the cases have worse EE under the stricter rate constraints. This phenomenon is caused by the additional energy cost of the artificial noise $\mathbf{z}$, which is the main factor in decreasing SINR of $R_l^{(\mathrm{E})}$.

5.2.5 The Effect of Transmitting Power P_{Max} on EE

The power resource budget is the guarantee of the network performance. However, unlimited usage of energy dissatisfies the requirements of green communications. In this part, we analyze its effects on the network EE. From Figure 8, all the performance differences from various cases are identical to the above results. For both $d_r = 42mm$ and $d_r = 52mm$, interestingly, the performance gaps between the HEA and the

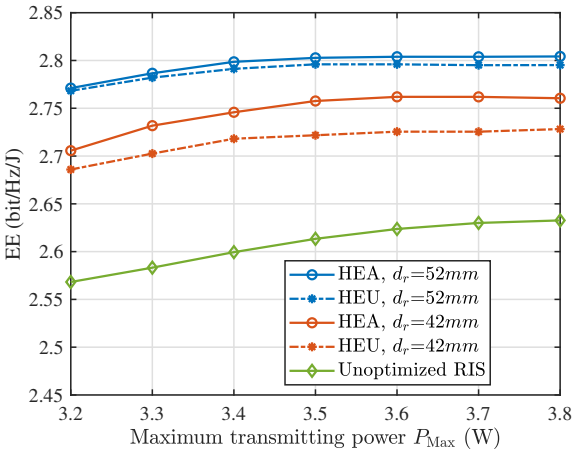

Figure 8. *The effect of transmitting power P_{Max} on EE.*

HEU shrink with the smaller power budgets. We consider this may come from multiple factors. The main reason could be that the hardware features perform a less important role in the channel reconstruction under the limited-power situation. Furthermore, the results also demonstrate that the EE will not keep growing with adding transmitting energy. In fact, power has two sides for the network EE, thus instead of continuously dissipating power, the algorithm will maintain a steady status as shown in Figure 8.

5.2.6 The Effect of Power Consumption P_I on EE

While the RIS is a nearly-passive device, there still is energy dissipation for element configurations. In particular, different power supply levels may be needed for the various circuits, hardware components, and op-

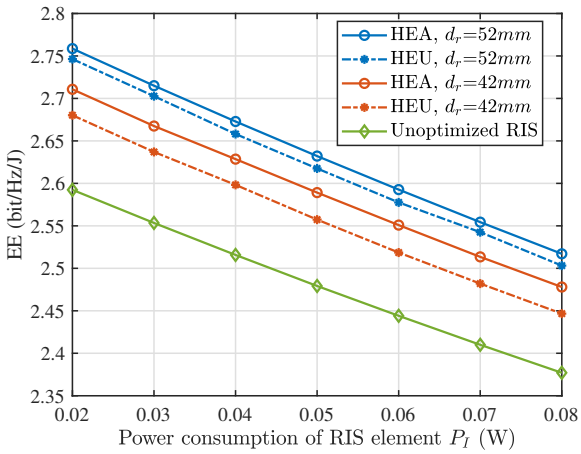

Figure 9. *The effect of power consumption P_I on EE.*

eration states of RIS. Therefore, the energy consumption P_I is analyzed in this part. As in Figure 9, the EE decreases almost linearly with the increased P_I due to the extra power requirements. Besides, the performance differences among cases are consistent with other figures.

All the simulation results prove the significance of the physical characteristics from the network perspective. Especially, the effects of the RIS with a more compact array, which is a typical choice in the practical deployment, should be considered carefully. During operation, easily ignoring them may cause performance loss.

VI. CONCLUSION

This paper investigated the RIS-enhanced SWIPT network. The S-parameter-based analysis approach was introduced to construct an end-to-end model, which includes the crucial physical features of all ends. With the model, an EE maximization problem constrained to the QoS requirements and physical limitations was formulated. Specifically, the security concern was presented by imposing restrictions on the unauthorized rate of the EHR. As for tackling the issue, an alternative strategy was adopted to separate the coupled variables. What's more, the load reflection coefficients of RIS were optimized through a novel BCD scheme based on the Sherman-Morrison formula. This approach takes the hardware features of RIS into account and can be seen as a strategy oriented to practical cases. Simulation results further proved the effectiveness of the proposed model and algorithms. Moreover, the hardware characteristics should not be ignored especially for the compact RIS-adied network. To describe the real communication system as closely as possible, the end-to-end model will be progressively extended in future works with incorporating more physical hardware components.

REFERENCES

[1] SHI W, XU W, YOU X, et al. Intelligent reflection enabling technologies for integrated and green internet-of-everything beyond 5G: Communication, sensing, and security[J]. IEEE Wireless Communications, 2023, 30(2): 147-154.

[2] MISRA N N, DIXIT Y, AL-MALLAHI A, et al. IoT, big data, and artificial intelligence in agriculture and food industry[J]. IEEE Internet of Things Journal, 2022, 9(9): 6305-6324.

[3] ZARGARI S, KHALILI A, WU Q, et al. Max-min fair energy-efficient beamforming design for intelligent reflecting surface-aided SWIPT systems with non-linear energy harvesting model[J]. IEEE Transactions on Vehicular Technology, 2021, 70(6): 5848-5864.

[4] PAN C, REN H, WANG K, et al. Intelligent reflecting surface aided MIMO broadcasting for simultaneous wireless information and power transfer[J]. IEEE Journal on Selected Areas in Communications, 2020, 38(8): 1719-1734.

[5] WU Q, ZHANG R. Joint active and passive beamforming optimization for intelligent reflecting surface assisted SWIPT under QoS constraints[J]. IEEE Journal on Selected Areas in Communications, 2020, 38(8): 1735-1748.

[6] FARA R, RATAJCZAK P, PHAN-HUY D T, et al. A prototype of reconfigurable intelligent surface with continuous control of the reflection phase[J]. IEEE Wireless Communications, 2022, 29(1): 70-77.

[7] JAAFAR W, BARIAH L, MUHAIDAT S, et al. Time-switching and phase-shifting control for RIS-assisted SWIPT communications[J]. IEEE Wireless Communications Letters, 2022, 11(8): 1728-1732.

[8] YU K, YU X, CAI J. UAVs assisted intelligent reflecting surfaces SWIPT system with statistical

CSI[J]. IEEE Journal of Selected Topics in Signal Processing, 2021, 15(5): 1095-1109.
[9] CAMANA M R, GARCIA C E, KOO I. Rate-splitting multiple access in a MISO SWIPT system assisted by an intelligent reflecting surface[J]. IEEE Transactions on Green Communications and Networking, 2022, 6(4): 2084-2099.
[10] LYU R, CHENG W. Joint reflection and power splitting optimization for RIS-assisted OAM-SWIPT[C]//GLOBECOM 2022-2022 IEEE Global Communications Conference. [S.l.]: IEEE, 2022: 1073-1078.
[11] WU Q, ZHANG R. Weighted sum power maximization for intelligent reflecting surface aided SWIPT[J]. IEEE Wireless Communications Letters, 2019, 9(5): 586-590.
[12] KHALILI A, ZARGARI S, WU Q, et al. Multi-objective resource allocation for IRS-aided SWIPT[J]. IEEE Wireless Communications Letters, 2021, 10(6): 1324-1328.
[13] GAO Y, WU Q, ZHANG G, et al. Beamforming optimization for active intelligent reflecting surface-aided SWIPT[J]. IEEE Transactions on Wireless Communications, 2023, 22(1): 362-378.
[14] ZHAO P, ZUO J, WEN C. Power allocation and beamforming vectors optimization in STAR-RIS assisted SWIPT[C]//2022 IEEE 22nd International Conference on Communication Technology (ICCT). [S.l.: s.n.], 2022: 1174-1178.
[15] ABRARDO A, DARDARI D, DI RENZO M, et al. MIMO interference channels assisted by reconfigurable intelligent surfaces: Mutual coupling aware sum-rate optimization based on a mutual impedance channel model[J]. IEEE Wireless Communications Letters, 2021, 10(12): 2624-2628.
[16] LI H, CAI W, LIU Y, et al. Intelligent reflecting surface enhanced wideband MIMO-OFDM communications: From practical model to reflection optimization[J]. IEEE Transactions on Communications, 2021, 69(7): 4807-4820.
[17] NAJAFI M, JAMALI V, SCHOBER R, et al. Physics-based modeling and scalable optimization of large intelligent reflecting surfaces[J]. IEEE Transactions on Communications, 2020, 69(4): 2673-2691.
[18] NAJAFI M, JAMALI V, SCHOBER R, et al. Physics-based modeling and scalable optimization of large intelligent reflecting surfaces[J]. IEEE Transactions on Communications, 2020, 69(4): 2673-2691.
[19] SHEN S, CLERCKX B, MURCH R. Modeling and architecture design of reconfigurable intelligent surfaces using scattering parameter network analysis[J]. IEEE Transactions on Wireless Communications, 2022, 21(2): 1229-1243.
[20] MORRIS M, JENSEN M. Network model for MIMO systems with coupled antennas and noisy amplifiers[J]. IEEE Transactions on Antennas and Propagation, 2005, 53(1): 545-552.
[21] DINKELBACH W. On nonlinear fractional programming[J]. Management science, 1967, 13(7): 492-498.
[22] PRESS W H. Numerical recipes 3rd edition: The art of scientific computing[M]. [S.l.]: Cambridge university press, 2007.

BIOGRAPHIES

Ruoyan Ma received the B.Eng. degree in human–computer interaction (HCI) from the South China University of Technology, China, in 2020. He is currently pursuing the Ph.D. degree with the School of Electronic and Information Engineering, South China University of Technology, China. His research interests include intelligent antenna system, reconfigurable intelligent surface, simultaneous wireless information and power transfer, electromagnetic theory, optimization theory and 6G networks.

Jie Tang (Senior Member, IEEE) received the B.Eng. degree from the South China University of Technology, China, the M.Sc. degree from the University of Bristol, U.K., and the Ph.D. degree from Loughborough University, U.K. From 2013 to 2015, he was a Research Associate at the School of Electrical and Electronic Engineering, The University of Manchester, U.K. He is currently a Professor at the School of Electronic and Information Engineering, South China University of Technology. His current research interests include SWIPT, UAV communications, NOMA, and reconfigurable intelligent surface. He received the IEEE ComSoc Asia-Pacific Outstanding Young Researcher Award in 2021. He was a co-recipient of Best Paper Awards at the ICNC 2018, CSPS 2018, WCSP 2019, 6GN 2020, and AICON2021.

Xiu Yin Zhang (Fellow, IEEE) received the B.S. degree in communication engineering from the Chongqing University of Posts and Telecommunications, Chongqing, China, in 2001, the M.S. degree in electronic engineering from the South China University of Technology, Guangzhou, China, in 2006, and the Ph.D. degree in electronic engineering from the City University of Hong Kong, Hong Kong, in 2009. Dr. Zhang is a fellow of the Institution of Engineering and Technology (IET). He was a recipient of the National Science Foundation for Distinguished Young Scholars of China. He won the First Prize of the 2016 Guangdong Provincial Natural Science Award and the 2021 Guangdong Provincial Technological Invention Award. He was a supervisor of several conference best paper award winners. He has served as the general chair/co-chair/technical program committee (TPC) chair/co-chair for a number of conferences. His research interests include antennas, RFIC, RF components and subsystems, and intelligent wireless communications and sensing.

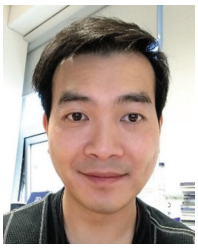

Kai-Kit Wong (Fellow, IEEE) received the B.Eng., M.Phil., and Ph.D. degrees in electrical and electronic engineering from The Hong Kong University of Science and Technology, Hong Kong, in 1996, 1998, and 2001, respectively. After graduation, he took up academic and research positions with The University of Hong Kong, Lucent Technologies, Bell-Labs, Holmdel, the Smart Antennas Research Group of Stanford University, and the University of Hull, U.K. He is currently the Chair of wireless communications with the Department of Electronic and Electrical Engineering, University College London, U.K. His current research centers around 5G and beyond mobile communications. He is fellow of IET. He was a co-recipient of the 2013 IEEE Signal Processing Letters Best Paper Award and the 2000 IEEE VTS Japan Chapter Award at the IEEE Vehicular Technology Conference in Japan in 2000, and a few other international best paper awards. He serves on the editorial board for several international journals.

Jonathon A. Chambers (Fellow, IEEE) received the Ph.D. and D.Sc. degrees in signal processing from the Imperial College of Science, Technology and Medicine (Imperial College London), London, U.K., in 1990 and 2014, respectively. Dr. Chambers is a fellow of the Royal Academy of Engineering, U.K., and the Institution of Electrical Engineers. In 2007, he received the first QinetiQ Visiting Fellowship for his outstanding contributions to adaptive signal processing and his contributions to QinetiQ, as a result of his successful industrial collaboration with the international defense systems company QinetiQ. He was the Technical Program Chair of the 15th International Conference on Digital Signal Processing and the 2009 IEEE Workshop on Statistical Signal Processing, both held at Cardiff, U.K., and the Technical Program Co-Chair of the 36th IEEE International Conference on Acoustics, Speech, and Signal Processing, Prague, Czech Republic. He has served on the IEEE Signal Processing Theory and Methods Technical Committee for six years and the IEEE Signal Processing Society Awards Board for three years, together with the Jack Kilby Award Committee. He was an Associate Editor for the IEEE TRANSACTIONS ON SIGNAL PROCESSING for two terms over the periods 1997–1999 and 2004–2007 and as a Senior Area Editor from 2011 to 2014.